ADVANCED FUNCTIONAL MATERIALS
www.afm-journal.de

Check for updates

Electroluminescent Solar Cells Based on $CsPbI_3$ Perovskite Quantum Dots

Yao Wang, Chenghao Duan, Xuliang Zhang, Jianguo Sun, Xufeng Ling, Junwei Shi, Long Hu, Zizhen Zhou, Xianxin Wu, Wei Han, Xinfeng Liu, Claudio Cazorla, Dewei Chu, Shujuan Huang, Tom Wu, Jianyu Yuan, and Wanli Ma**

All-inorganic $CsPbX_3$ (X = Cl, Br, I, or mixed halides) perovskite quantum dots (QDs) exhibit tunable optical bandgaps and narrow emission peaks, which have received worldwide interest in the field of both photovoltaics (PVs) and light-emitting diodes (LEDs). Herein, it is reported a discovery that $CsPbI_3$ perovskite QD solar cell can simultaneously deliver high PV performance and intense electroluminescence. In specific, the multifunctional $CsPbI_3$ QD film is fabricated through a simple yet efficient solid-state-ligand exchange process using a tailored organic ligand triphenyl phosphite (TPPI). The function of QD surface manipulation using TPPI here is proven to be twofold, balancing the carrier transport and effectively passivating the QD surface to produce conductive and emissive QD film. The $CsPbI_3$ perovskite QD solar cell delivers a champion efficiency of 15.21% with improved open circuit voltage and high fill factor. Concurrently functioning as a red LED, the $CsPbI_3$ perovskite QD solar cell outputs electric power to light conversion efficiency approaching 4%, a record value for QD electroluminescent PVs. The results here indicate that these versatile perovskite QDs may be a promising candidate for fabricating multifunctional optoelectronic devices.

1. Introduction

Metal halide perovskite quantum dots (QDs) offer high defect tolerance and expanded compositional and bandgap tunability over conventional metal chalcogenide QDs.[1–4] In addition, these emerging perovskite QDs, with room-temperature deposition processing, tunable surface chemistry, and crystallographic stabilization,[5–9] provide additional benefits compared to their polycrystalline film counterparts. During the past 5 years, tremendous efforts have been made toward the applications of perovskite QDs as photosensitive materials for photovoltaics (PVs),[10–13] detectors,[14] light emitters for displays,[15] light-emitting diodes (LEDs),[16,17] and other functional devices.

In 2015, the discovery of cesium lead halide all-inorganic perovskite QDs ($CsPbX_3$, X = Cl, Br, I, or mixed halides) paved a new avenue for QD optoelectronic technology.[2,3] The as-synthesized $CsPbX_3$ QDs exhibit over 90% photoluminescence quantum yield (PLQY) with narrow emission peak, and tunable PL from deep blue to far red by simply adjusting the halide composition or QD size.[18–20] Initially, these all-inorganic colloidal perovskite QDs with high PLQY were widely studied for potential LED and display applications. While for PV application, the most suitable candidate in this family is $CsPbI_3$ because of its desired optical bandgap of 1.73 eV. In 2017, the PV efficiency of $CsPbI_3$ QDs reached a certified value of 13.4%, surpassing all other QD PVs.[21] And the power conversion efficiency (PCE) has been further enhanced to over 15% through QD surface

Y. Wang, X. Zhang, J. Sun, X. Ling, J. Shi, J. Yuan, W. Ma
Institute of Functional Nano and Soft Materials (FUNSOM)
Jiangsu Key Laboratory for Carbon-Based Functional Materials and Devices
Soochow University
199 Ren-Ai Road, Suzhou Industrial Park, Suzhou, Jiangsu 215123, P. R. China
E-mail: jyyuan@suda.edu.cn; wlma@suda.edu.cn

C. Duan
School of Environment and Energy
South China University of Technology
Guangzhou 510640, P. R. China

L. Hu, S. Huang
School of Engineering
Macquarie University
Sydney, New South Wales 2109, Australia

The ORCID identification number(s) for the author(s) of this article can be found under https://doi.org/10.1002/adfm.202108615.

DOI: 10.1002/adfm.202108615

Z. Zhou, D. Chu, T. Wu
School of Materials Science and Engineering
University of New South Wales (UNSW)
Sydney, New South Wales 2052, Australia

X. Wu, X. Liu
CAS Key Laboratory of Standardization and Measurement for Nanotechnology
CAS Center for Excellence in Nanoscience
National Center for Nanoscience and Technology
Chinese Academy of Sciences
Beijing 100190, P. R. China

W. Han
Department of Chemistry
Baotou Teachers' College
Baotou 014030, P. R. China

C. Cazorla
Departament de Física
Universitat Politècnica de Catalunya
Campus Nord B4-B5, Barcelona E-08034, Spain

 © 2021 Wiley-VCH GmbH

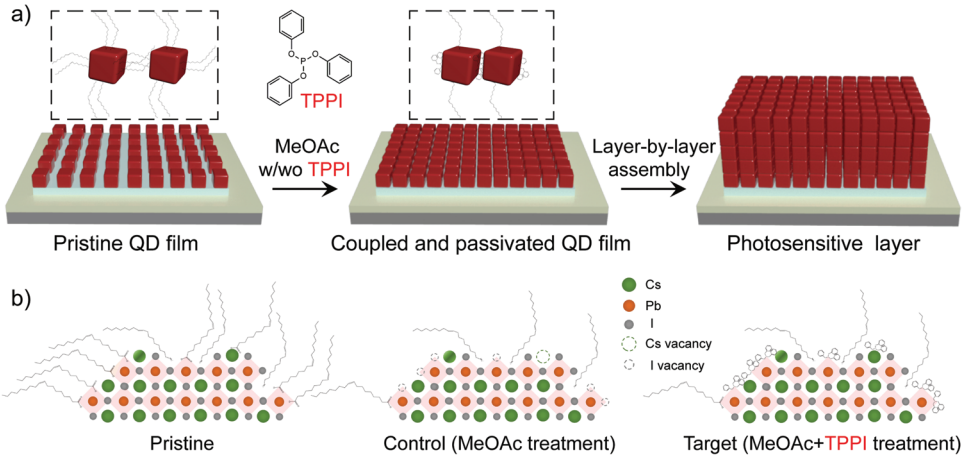

Figure 1. a) The schematic of the preparation for $CsPbI_3$ QD photosensitive layer treated by MeOAc with or without (w/wo) TPPI. b) The surface of as-synthesized $CsPbI_3$ QDs, treated by MeOAc w/wo TPPI, which are defined as pristine, control, and target film, respectively.

passivation and ligand manipulation.[7,22,23] Meanwhile, these passivating strategies were also employed to develop efficient red LED devices using $CsPbI_3$ QDs and the highest electroluminescent external quantum efficiency (EQE_{EL}) value over 20% has been reported, representing the state-of-the-art red LEDs.[24] Although the PV efficiency of $CsPbI_3$ QDs still lags behind their polycrystalline film counterparts, $CsPbI_3$ QD film potentially offers higher emissive properties than their bulk thin-film counterparts because of its more tunable surface chemistry. This feature is extremely important for designing an electroluminescent solar cell, which has been reported in organic and thin-film perovskite solar cells,[25–27] however, there is barely any experimental evidence proving electroluminescent QD PVs.

In this work, we discovered that perovskite QDs can be attractive in achieving both very high solar-to-electric PCE as well as electric power to light conversion efficiency. We first reported the QD electroluminescent solar cell using $CsPbI_3$ QDs through incorporating a tailored functional organic ligand triphenyl phosphite (TPPI). Herein, the purpose of QD surface manipulation was found to be different from the conventional scenarios. The deployment of bulky conductive ligand can concurrently balance carrier transport and enable surface passivation, which can presumably produce emissive QD films for PV application. Organic phosphorus is a kind of strong bonding ligand (interaction between P and Pb) that has been tried in chalcogenide QDs.[28] The selected ligand TPPI can well match these guidelines, by fabricating device using TPPI-treated $CsPbI_3$ QDs; our study showed that the QD device exhibits a high PV efficiency of 15.21% mainly due to enhanced open-circuit voltage (V_{oc}) and fill factor (FF). More interestingly, benefitting from the effective QD surface passivation using TPPI, the $CsPbI_3$ QD solar cell also demonstrated a decent red LED performance with a high EQE_{EL} approaching 4.0%, which is the highest value reported so far for electroluminescent QD PVs.

2. Results and Discussion

$CsPbI_3$ QDs capped with organic long ligands were synthesized and purified according to the hot-injection method reported previously.[29] The purified QD solids were finally dispersed in octane at a concentration of 70 mg mL^{-1} for solar cell fabrication. We further characterized the QDs using transmission electron microscopy (Figure S1, Supporting Information), UV–vis absorption, PL (Figure S2, Supporting Information), and X-ray diffraction (Figure S3, Supporting Information). All these results demonstrate that we have successfully obtained cubic $CsPbI_3$ QDs with uniform size and distribution (average size ≈ 10 nm). **Figure 1**a illustrates the $CsPbI_3$ QD film deposition process for device fabrication using the conventional layer-by-layer methodology. For the preparation of each $CsPbI_3$ QD film, polar solvent methyl acetate (MeOAc) was adopted to post-treat the as-prepared QD arrays to partly remove the native long-chain ligands. For the target device, MeOAc with optimal TPPI was applied to remove surface ligands and passivate the surface defects. As shown in Figure 1b, the surface of MeOAc-treated $CsPbI_3$ QDs is still covered with native organic long ligands and surface vacancies. We anticipate that the addition of TPPI during the solid-state-ligand exchange process would offer two major merits: One is surface vacancy filling; the other is bonding with undercoordinated ions, eventually stabilizing the QD and reducing trap states.

To explore the change of QD surface environment, Fourier transform infrared (FTIR) characterization was first adopted. As shown in **Figure 2**a, for the control film treated by neat MeOAc, the signal responses are obviously observed with features at 1464 cm^{-1} (C—H_2), 2762–2985 cm^{-1} (C—H_x), and 3005 cm^{-1} (C=C—H) representing oleyl groups derived from the oleate (OA^-) and oleylammonium (OLA^+) ligands.[30] The broad response between 3122 and 3267 cm^{-2} (NH_3^+) represents OLA^+.[31] Besides, the features at 1583 cm^{-1} (C=O), 1406 cm^{-1} (COO^-), and 1529 cm^{-1} (COO^-) represent OA^-.[5,32,33] For the target film, the peak intensity associated with OA^- and OLA^+ is similar to that of the control one. In addition, distinct resonances in the broad response between 1145 and 1220 cm^{-1} were observed, which is ascribed to the stretching vibration of C—O—(P),[34–36] indicating the existence of TPPI in the target QD film. More direct evidence is provided by X-ray photoelectron spectroscopy (XPS) characterization. The intensity of O 1s core-level spectra is significantly increased after TPPI treatment

© 2021 Wiley-VCH GmbH

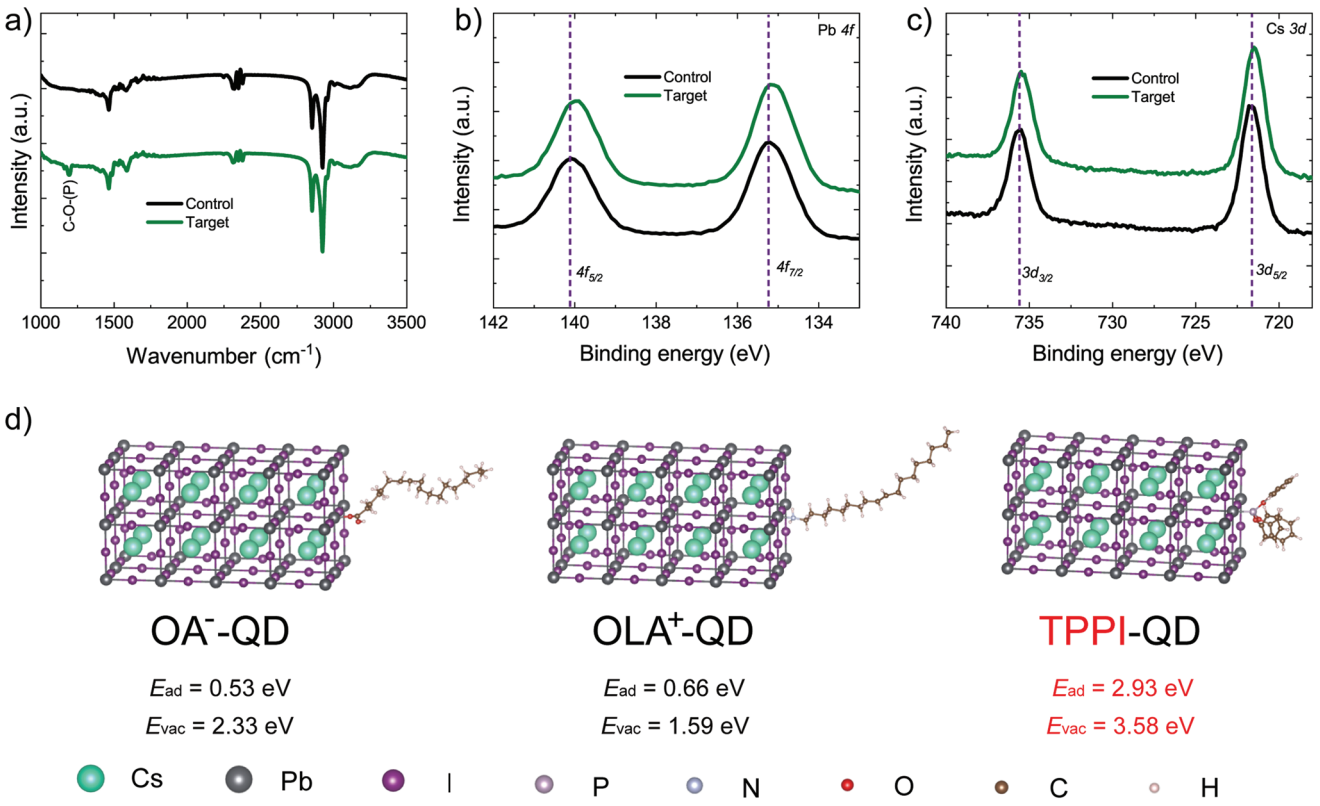

Figure 2. a) FTIR spectra of control and target $CsPbI_3$ QD films deposited on CaF_2 substrate. XPS spectra of b) Pb 4f and c) Cs 3d for control and target $CsPbI_3$ QD films deposited on glass/FTO substrate. d) First-principles density functional theory results. Estimated adsorption energy (E_{ad}) of the OA^-, OLA^+, and TPPI ligands on the optimized $CsPbI_3$ QD surfaces, and the corresponding formation energy of surface I vacancies (E_{vac}).

(Figure S4a, Supporting Information). Figure 2b,c displays the XPS spectra of Pb 4f and Cs 3d. All peaks shift to lower binding energy after the TPPI treatment, indicating the increase of electron density around the Pb and Cs atoms, because the outermost vacant orbits of Pb^{2+} and Cs^+ can be occupied by the lone pair electrons of P atoms in TPPI, thereby promoting the formation of chemical bonding between Pb^{2+}/Cs^+ and organic ligand TPPI. In the core level spectra of I (Figure S4c, Supporting Information), we did not observe any shift before and after the TPPI treatment, indicating less chemical interaction between TPPI and I^-. To further understand the nature of the bonding of TPPI, OA^-, and OLA^+ ligands to the QD surface, we performed density functional theory (DFT) calculations with the results shown in Figure 2d. Our DFT calculations indicate that the TPPI ligands bind most strongly to the $CsPbI_3$ QD surface (through the formation of bonds between TPPI-P and $CsPbI_3$-Pb atoms shown in Figure S5, Supporting Information). In specific, we estimated an adsorption energy (E_{ad}) of 2.9 eV for TPPI, of 0.5 eV for OA^-, and of 0.7 eV for OLA^+. The huge E_{ad} value estimated for TPPI suggests the possibility of QD surface stabilization via the reduction of surface distortion. To assess the effect on QD passivation induced by the presence of the OA^-, OLA^+, and TPPI ligands, we calculated the corresponding formation energy of surface I vacancies (E_{vac}). The largest E_{vac} value was obtained for TPPI, namely, 3.6 eV, which is significantly higher than the E_{vac} values obtained for OA^- (2.3 eV) and OLA^+ (1.6 eV). Meanwhile, the E_{vac} value obtained in the absence of any molecular ligand is around 1.4 eV. These outcomes indicate that retention of I ions at the QD surface becomes energetically most favorable in the presence of TPPI ligands. The unraveled TPPI-induced I surface stabilization also allows the halide perovskite to retain its cubic symmetry.

To understand the TPPI treatment on the optoelectronic properties, a regular planar n–i–p device architecture of glass/fluorine-doped tin oxide (FTO)/TiO_2/$CsPbI_3$ QDs/poly(triarylamine) (PTAA)/MoO_3/Ag was employed (**Figure 3**a), and each layer is clearly identified in the cross-sectional scanning electron microscopy (SEM) image. Figure 3b presents the current density versus voltage (J–V) characteristics of the optimal solar cells using the MeOAc post-treatment process with or without TPPI, under AM 1.5G illumination at an intensity of 100 mW cm^{-2}. The performance parameters of the device are shown in **Table 1**. The best PCE of 13.54% was achieved for the control device, and the efficiency was further enhanced to 15.21% (14.97% at the maximum power point) for the target device (The forward scan and reverse scan J–V curves are shown in Figure S6, Supporting Information), which is mainly due to increased V_{oc} (1.23 V) and FF (79.45%). The PCE distributions of 20 devices for each case are shown in Figure 3c, validating the consistent performance enhancement of the device. It is worth noting that short organic ligand exchange or passivation can enhance the electronic coupling between neighboring QDs and then significantly improve the short circuit current density (J_{sc}). However, we did not witness any significant enhancement of J_{sc} before and after the TPPI

© 2021 Wiley-VCH GmbH

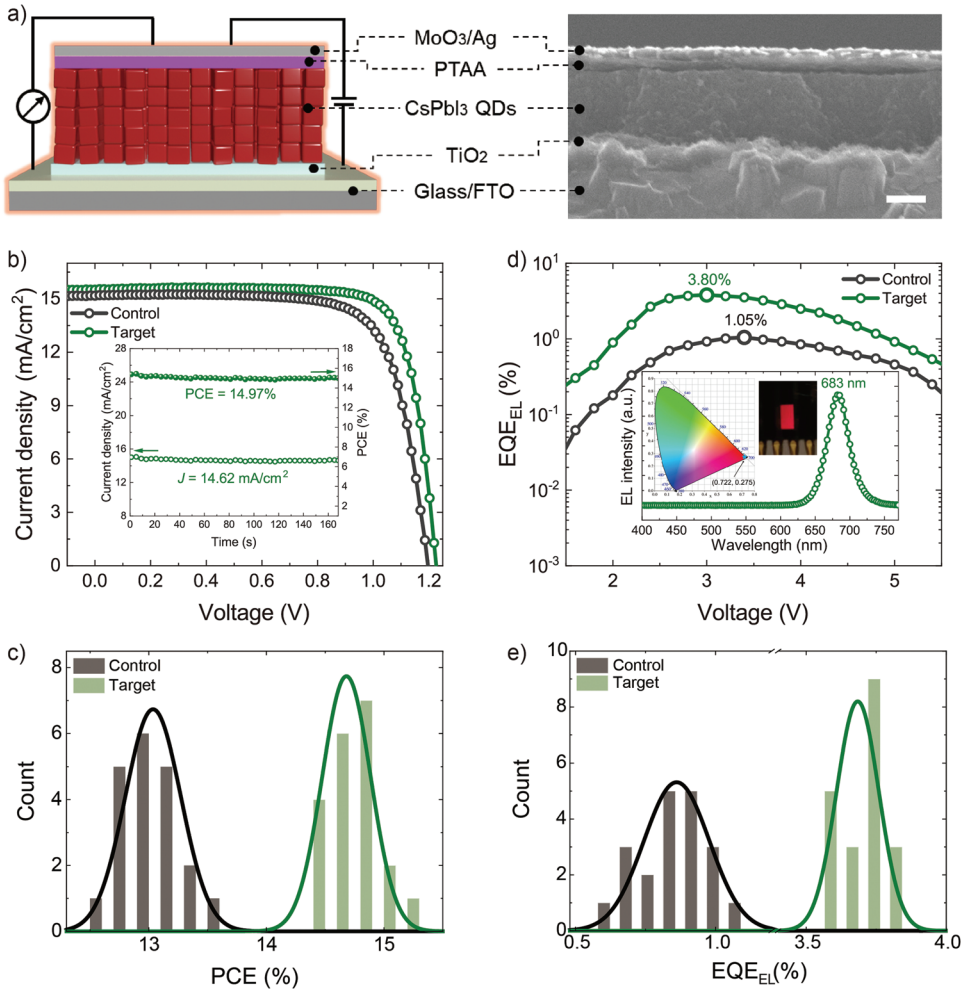

Figure 3. a) Illustration and cross-sectional SEM image of $CsPbI_3$ QD electroluminescent solar cell (scale bar: 100 nm). b) *J–V* curves of the control and target $CsPbI_3$ QD electroluminescent solar cells; the insert is the steady power output (SPO) of the target $CsPbI_3$ QD solar cell. c) PCE histograms of the control and target device, which were obtained from 20 devices for each case. d) Electroluminescent EQEs of the control and target $CsPbI_3$ QD solar cells; insert is the electroluminescence, chromaticity diagram, and photograph of the target device. e) EQE_{EL} histograms of the control and target $CsPbI_3$ QD devices, which were obtained from 20 devices for each case.

treatment. Meanwhile, EQE of the target device was performed with the result shown in Figure S7, Supporting Information, and an integrated J_{sc} of 15.30 mA cm^{-2} was obtained (control one is 15.13 mA cm^{-2}), confirming that the enhancement of the PCE is mainly due to V_{oc} and FF.

The higher V_{oc} of the target device motivated us to study the energy loss to get insight into the potential of TPPI treatment. We first investigated the relationship between EQE_{EL} and current density for the solar cells (Figure S8, Supporting Information). At the position of driving current density corresponding to the J_{sc} measured under 1 sun illumination, the control and target devices exhibit a EQE_{EL} values of 1.81% and 0.58%, respectively, indicating that TPPI passivation can effectively reduce the nonradiative recombination.[37,38] In this context, we determined the nonradiation open-circuit voltage loss ($\Delta V_{oc}^{non\text{-}rad}$) with the following equation:[38]

$$\Delta V_{oc}^{non-rad} = -\frac{nkT}{q}\ln(EQE_{EL}) \quad (1)$$

The $\Delta V_{oc}^{non\text{-}rad}$ is found to be 206 and 133 meV for the control and the target device, respectively. These results indicate that the TPPI-treated QD film is beneficial for achieving a low voltage deficit, and such rational surface ligand manipulation can reduce $\Delta V_{oc}^{non\text{-}rad}$ toward higher V_{oc}.

Meanwhile, we characterized the LED performance of both control and target PV devices. As shown in Figure S9, Supporting Information, in terms of brightness, the target $CsPbI_3$ QD PV device has the maximum luminance of 47.01 W sr^{-1} m^{-2} under an applied voltage of 4.0 V, which is over four times higher than the control device (11.04 W sr^{-1} m^{-2} under the same applied voltage). Moreover, as shown in Figure 3d, the target PV device has a remarkable maximum EQE_{EL} of 3.80% at the applied voltage of 3.0 V, significantly higher than that of the control PV device (EQE_{EL} = 1.05%). As shown in Figure 3d, the target solar cell exhibits sharp electroluminescence peak at the wavelength of 683 nm with a full width at half maximum around 30 nm. Figure 3d shows the chromaticity diagram which reveals the optical color information of the target device,

© 2021 Wiley-VCH GmbH

Table 1. Device parameters of the $CsPbI_3$ QD solar cells; the average values were summarized from 20 parallel devices.

		V_{oc} [V]	J_{sc} [mA cm^{-2}]	FF [%]	PCE [%]	EQE_{EL} [%]
Control	Average	1.19 ± 0.03	15.06 ± 0.40	72.46 ± 2.44	13.05 ± 0.50	0.86 ± 0.21
	Champion	1.20	15.15	74.49	13.55	1.05
Target	Average	1.22 ± 0.02	15.31 ± 0.45	78.31 ± 1.96	14.68 ± 0.45	3.68 ± 0.13
	Champion	1.23	15.54	79.45	15.21	3.80

a feature quite ideal for red display applications. A photograph of the LED (inset in Figure 3d) also shows its red-light emission. The EQE_{EL} distributions of 20 devices for each case are shown in Figure 3e, validating the LED performance enhancement. In should be noted that we report here for the first time a QD solar cell device that exhibits both very high solar-to-electric PCE and intense electroluminescence. An EQE_{EL} of 3.80% is the highest reported value for any QD solar cells up to now. More importantly, these results indicate that surface ligand manipulation can prepare high-quality perovskite QD films with balanced transport and injection of electrons and holes, demonstrating great potential for developing highly efficient electroluminescent solar cells.

In order to further understand the mechanism behind the device improvement, more characterization techniques were employed. The effect of TPPI treatment on surface morphology and crystal structure properties of $CsPbI_3$ QD film was first investigated. The top-view SEM images in **Figure 4**a,b clearly

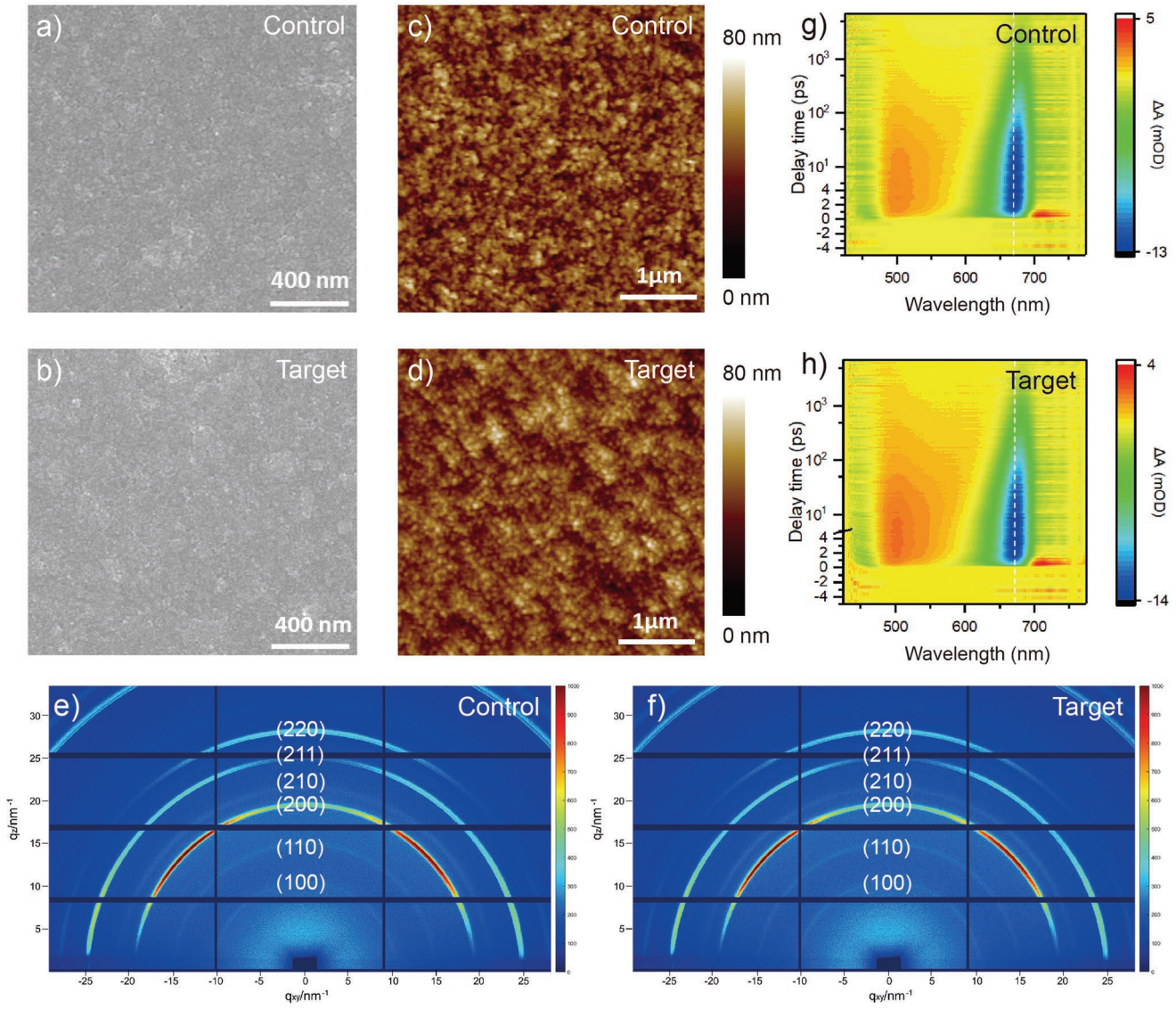

Figure 4. a,b) Top SEM images, c,d) AFM height images, e,f) 2D GIWAXS patterns, and g,h) 2D fs-TA plots of control and target $CsPbI_3$ QD films.

© 2021 Wiley-VCH GmbH

show that the TPPI treatment produces a denser QD film with reduced pin-holes. A similar trend is also found in the atomic force microscopy height images (Figure 4c,d). The TPPI-treated film shows a smoother surface morphology (roughness: 9.8 nm) compared to the neat MeOAc-treated one (roughness: 10.6 nm). Then, the crystalline nature of $CsPbI_3$ QDs in the as-prepared $CsPbI_3$ QD film was evaluated by synchrotron-based 2D grazing-incidence wide-angle X-ray scattering (GIWAXS). As shown in Figure 4e,f, both samples exhibit strong X-ray characteristic diffractions of QDs. We observed apparent diffraction peaks of (100), (110), (200), (210), (211), and (220) at preferable positions for the $CsPbI_3$ QD films w/wo TPPI, indicating both QD films have high crystallinity and the TPPI treatment exerted a negligible effect on QD assembling and packing.

Moreover, femtosecond transient absorption (fs-TA) was applied to understand the relationship between the QD film morphology and the carrier dynamics. Figure 4g,h depicts the 2D fs-TA plots for the control and target QD films, respectively, in which the distinct peak (dashed white line) located at ≈680 nm corresponds to the ground-state bleaching (GSB) of the first excitonic transition. The GSB decay dynamics (Figure S10 and Table S2, Supporting Information) of both films were fitted by three exponential components of τ_1, τ_2, and τ_3, corresponding to the timescale of hot-phonon bottleneck, Auger recombination, and trap states recombination, respectively.[39,40] The target $CsPbI_3$ QD film treated with TPPI possess longer decay time associated with trap states relative to the control one, demonstrating that TPPI can effectively passivate surface trap states and is beneficial for reducing nonradiative recombination in $CsPbI_3$ QD film.

Steady-state PL and time-resolved PL (TRPL) were introduced to study the carrier dynamics. We also investigated the pristine $CsPbI_3$ QD film for a thorough comparison. As shown in **Figure 5**a, compared to the pristine film, the control QD film exhibits a red-shifted PL peak (The same trend can also be observed in the UV–vis absorption spectra as shown in Figure S11, Supporting Information) with significantly decreased intensity, indicating improved electronic coupling with increased surface defects after surface ligand removal. After the TPPI treatment, we observed the same red shift while significantly improving PL intensity, suggesting effective QD surface defects passivation enabled by TPPI. In the PL decay profile shown in Figure 5b, the TPPI-treated target film exhibitsthe longest lifetome up to 6.5 ns, confirming that TPPI can reduce the density of surface trap states, thereby reducing nonradiative recombination. To gain insight into the change of trap states density, the electron-only devices with the structure of FTO/TiO_2/$CsPbI_3$ PQD/$PC_{61}BM$/Ag (Figure S12, Supporting Information) were applied with the results shown in Figure 5c. The control $CsPbI_3$ QD film possesses a density of electronic trap states (n_e) value of 2.38×10^{11} cm^{-3}, which is higher than that of TPPI-treated device (n_e value of 1.56×10^{11} cm^{-3}), consistent with the PL and TRPL results. In addition, the TPPI-treated $CsPbI_3$ QD film presents a higher electronic mobility (μ_e) of 0.857 cm^2 V^{-1} s^{-1} compared to that of 0.353 cm^2 V^{-1} s^{-} in the control one, which may be due to the reduction of surface trap states.

Finally, we characterized the control and target $CsPbI_3$ QD electroluminescent solar cells to correlate the improved carrier dynamics with device performance. The photocurrent density (J_{ph}) against the effective voltage (V_{eff}) was recorded in Figure S13, Supporting Information. At low V_{eff}, J_{ph} linearly increases with V_{eff}, and the target device presents a higher J_{ph} relative to the control one in the same V_{eff} range, indicating that the TPPI passivation is beneficial for carrier extraction.[41,42] Moreover, the changes of J_{sc} and V_{oc} as a function of illumination intensity (I) were recorded and the results were shown in Figure S14, Supporting Information, and Figure 5d. The control and target devices show exponential factor (α) values of 0.98 and 0.99, respectively, demonstrating that both devices exhibit negligible bimolecular recombination at short-circuit conditions.[39] In comparison, the slope of the target device for the V_{oc} measurements is $1.31kT/q$, which is lower than that of the control device ($1.49kT/q$), indicating that the trap-assisted carrier recombination has been effectively suppressed through the TPPI passivation.[43] Figure 5e shows the electrochemical impedance spectroscopy result to obtain the transfer resistance (R_{tr}) and recombination resistance (R_{rec}).[44] In comparison with the control device treated by neat MeOAc, the target device shows a reduced R_{tr} (76.2 Ω) and an increased R_{rec} (507.8 Ω), suggesting that TPPI can suppress the carrier recombination and improve the charge transfer in the solar cell device. In addition, transient photovoltage, performed at open-circuit condition, was introduced, as shown in Figure 5f. The target device shows a photovoltage decay time of 1.72 ms, longer than that of 1.22 ms for the control device. Larger photovoltage decay time suggests that TPPI passivation can reduce subbandgap trap states, thereby suppressing nonradiation recombination.

To deeply understand the origin of the enhanced V_{oc} and FF in the target device, a series of device comparison results, derived from the J–V curves in Figure 3b, are shown in Figure 5g–i, with the detailed information presented in the Supporting Information. The values of shunt conductance (G) for both the control and target QD devices (Figure 5g) approach 0 mS cm^{-2}, indicating that as-prepared $CsPbI_3$ QD devices in this research possess negligible leakage current when working under illumination.[45,46] As shown in Figure 5h, the ideality factor (n) of the target device is 2.30, which is slightly lower than that of the control one (2.88), indicating TPPI passivation is beneficial for improving charge transfer and suppressing charge recombination due to the reduction of defect states at the QD surface.[47,48] In addition, the target device displays a reduced series resistance (R_s) of 1.71 Ω cm^{-2} compared to the control device with a R_s value of 2.50 Ω cm^{-2}, demonstrating that TPPI passivation enables better interfacial contact for higher FF (Figure 5h).[49] Finally, Figure 5i shows that the saturated recombination current density (J_0) of the target device (2.86×10^{-7} mA cm^{-2}) is lower than that of the control one (2.83×10^{-6} mA cm^{-2}), indicating suppressed recombination for higher V_{oc} through TPPI passivation.[47,50]

3. Conclusion

In summary, we report the first electroluminescent QD solar cell based on $CsPbI_3$ QDs. Through adopting a strong organic ligand TPPI, we have successfully produced $CsPbI_3$ QD films which exhibit both very high solar-to-electric PCE and intense electroluminescence. The device with the target $CsPbI_3$ QD

© 2021 Wiley-VCH GmbH

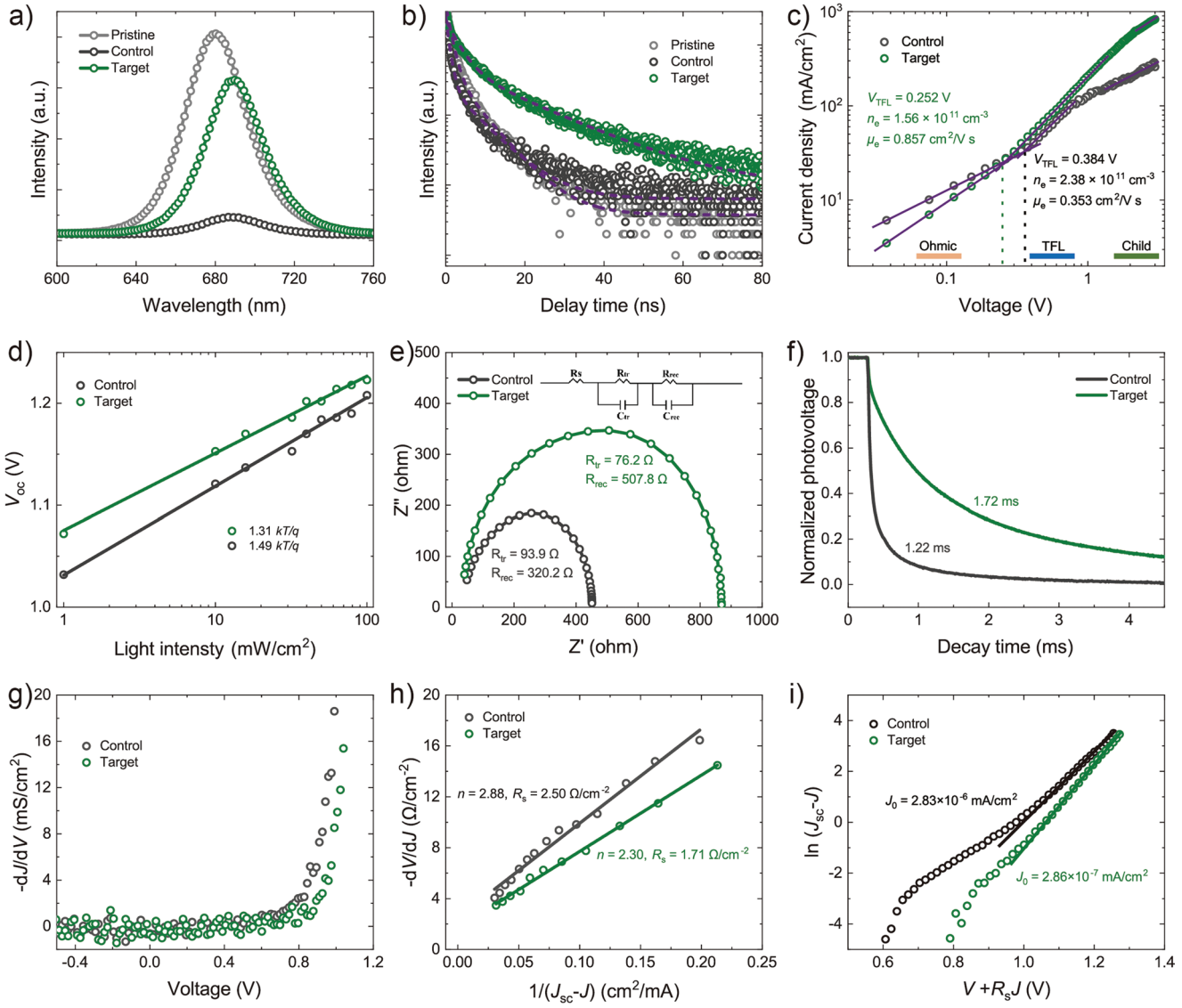

Figure 5. a) PL and b) TRPL spectra of pristine, control, and target $CsPbI_3$ QD films. The excitation wavelengths of PL and TRPL are 390 and 455 nm respectively. c) *J*–*V* curves of the control and target $CsPbI_3$ QD electronic-only devices. d) Changes of V_{oc} along with light intensity, e) Nyquist plots (Inserted picture is equivalent circuit model), and f) TPV spectra of the control and target $CsPbI_3$ QD electroluminescent solar cells. g) The relationship of $-\frac{dJ}{dV}$ with respect to voltage. h) Plot of $-\frac{dV}{dJ}$ with respect to $1/(J_{sc}-J)$, and i) plot of $\ln(J_{sc}-J)$ with respect to $V+R_sJ$, which was derived from Figure 3b.

photosensitive layer treated by pure MeOAc with TPPI can obtain a best PCE of 15.21% as well as a peak LED EQE_{EL} of 3.80%. The functional phosphorus ligand exhibits strong bonding to the QD surface, and such bulky conductive ligand can further balance carrier transport as well as enable surface passivation. As a result, the electrical coupling between $CsPbI_3$ QDs is enhanced, leading to improved charge transport, reduced carrier recombination, and then simultaneous high PV efficiency and LED EQE_{EL}. To the best of our knowledge, this is the first report of the electroluminescent solar cell using QDs, and the unique tunability of surface chemistry may be generalized to advance multifunctional QD-based optoelectronic devices.

4. Experimental Section

Preparation and Characterization of $CsPbI_3$ Quantum Dot Electroluminescent Solar Cell: First, a TiO_2 compact electronic transporting layer was deposited on the FTO substrate by the method of chemical bath deposition according to the previous report.[51] Second, the as-prepared FTO/TiO_2 substrate was transferred to a glovebox filled by dry air with the relative humidity of ≈10%. 70 mg mL^{-1} of *n*-octane dispersion of $CsPbI_3$ QDs was deposited on the FTO/TiO_2 substrate with two-step spin coating of 1000 rpm for 15 s and 2000 rpm for 20 s. The mixed solvent of TPPI and MeOAc with a concentration of 0.32 mg mL^{-1} was dropped on the substrate for 5 s followed by soaking in pure MeOAc for 5 s. The step was repeated for five times to prepare a $CsPbI_3$ QD photo-active layer with sufficient thickness. Then, the substrate was successively soaked in a saturated solution of ethyl acetate of FAI and pure MeOAc for 3 s,

© 2021 Wiley-VCH GmbH

respectively. Third, the as-prepared FTO/TiO_2/$CsPbI_3$ QDs substrate was transferred to a glovebox which was filled by pure nitrogen, to deposite 15 mg mL^{-1} of toluene solution of tris(pentafluorophenyl)borane-doped PTAA to prepare hole transporting layer, followed by transferring the sample into thermal evaporation equipment with the purpose of depositing 8 nm of MoO_3 and 120 nm of Ag electrode under a vacuum of 2×10^{-6} mbar. The current density–voltage (*J–V*) characteristics of the solar cells was measured using a Keithley 2400 Digital Source Meter under N_2 glovebox and simulated AM 1.5G spectrum at 100 mW cm^{-2} with a solar simulator (Class AAA, 94023A-U, Newport). Before test, the light intensity of the Xenon lamp was calibrated with a standard silicon solar cell (91150V, Newport Oriel). *J–V* scans were measured by the forward direction (–1.3 to 1.3 V) and reverse direction (1.3 to –1.3 V) with the speed of 0.016 V per point and a scan rate of 0.1 V s^{-1}. The active area of 7.25 mm^2 was defined by a shadow mask. The EQE measurement of the solar cells was characterized on a Solar Cell Scan 100 system (Zolix Instruments Co. Ltd.).

Supporting Information

Supporting Information is available from the Wiley Online Library or from the author.

Acknowledgements

This work was supported by the National Key Research and Development Program of China (2019YFE0108600), National Natural Science Foundation of China (52073198, 22161142003, and 61911530158), Natural Science Foundation of Jiangsu Province (BK20211598), Science and Technology Program of Jiangsu Province (BZ2020011), Science and Technology Program of Suzhou (SYG202037), "111" project, the China Postdoctoral Science Foundation (Grant No. 2021T140495), Collaborative Innovation Center of Suzhou Nano Science and Technology, Soochow University, and National Natural Science Foundation of Jiangsu Province (No. BK20211598).

Conflict of Interest

The authors declare no conflict of interest.

Data Availability Statement

Research data are not shared.

Keywords

$CsPbI_3$, electroluminescent solar cells, perovskite quantum dots, surface passivation, triphenyl phosphite

Received: August 27, 2021
Revised: October 5, 2021
Published online:

[1] T. J. Milstein, D. M. Kroupa, D. R. Gamelin, *Nano Lett.* **2018**, *18*, 3792.
[2] L. Protesescu, S. Yakunin, M. I. Bodnarchuk, F. Krieg, R. Caputo, C. H. Hendon, R. X. Yang, A. Walsh, M. V. Kovalenko, *Nano Lett.* **2015**, *15*, 3692.
[3] G. Nedelcu, L. Protesescu, S. Yakunin, M. I. Bodnarchuk, M. J. Grotevent, M. V. Kovalenko, *Nano Lett.* **2015**, *15*, 5635.
[4] J. De Roo, M. Ibanez, P. Geiregat, G. Nedelcu, W. Walravens, J. Maes, J. C. Martins, I. Van Driessche, M. V. Kovalenko, Z. Hens, *ACS Nano* **2016**, *10*, 2071.
[5] L. M. Wheeler, E. M. Sanehira, A. R. Marshall, P. Schulz, M. Suri, N. C. Anderson, J. A. Christians, D. Nordlund, D. Sokaras, T. Kroll, S. P. Harvey, J. J. Berry, L. Y. Lin, J. M. Luther, *J. Am. Chem. Soc.* **2018**, *140*, 10504.
[6] J. Shi, F. Li, Y. Jin, C. Liu, B. Cohen-Kleinstein, S. Yuan, Y. Li, Z. K. Wang, J. Yuan, W. Ma, *Angew. Chem., Int. Ed.* **2020**, *59*, 22230.
[7] X. Ling, J. Yuan, X. Zhang, Y. Qian, S. M. Zakeeruddin, B. W. Larson, Q. Zhao, J. Shi, J. Yang, K. Ji, Y. Zhang, Y. Wang, C. Zhang, S. Duhm, J. M. Luther, M. Gratzel, W. Ma, *Adv. Mater.* **2020**, *32*, 2001906.
[8] Y. Wang, J. Yuan, X. Zhang, X. Ling, B. W. Larson, Q. Zhao, Y. Yang, Y. Shi, J. M. Luther, W. Ma, *Adv. Mater.* **2020**, *32*, 2000449.
[9] J. Yuan, A. Hazarika, Q. Zhao, X. Ling, J. M. Luther, *Joule* **2020**, *4*, 1160.
[10] J. Yuan, X. Zhang, J. Sun, R. Patterson, H. Yao, D. Xue, Y. Wang, K. Ji, L. Hu, S. Huang, D. Chu, T. Wu, J. Hou, J. Yuan, *Adv. Funct. Mater.* **2021**, *31*, 2101272.
[11] J. Yuan, N. Rujisamphan, W. Ma, J. Yuan, Y. Li, S.-T. Lee, *J. Energy Chem.* **2021**, *62*, 505.
[12] K. Chen, W. Jin, Y. Zhang, T. Yang, P. Reiss, Q. Zhong, U. Bach, Q. Li, Y. Wang, H. Zhang, Q. Bao, Y. Liu, *J. Am. Chem. Soc.* **2020**, *142*, 3775.
[13] D. Jia, J. Chen, M. Yu, J. Liu, E. M. J. Johansson, A. Hagfeldt, X. Zhang, *Small* **2020**, *16*, 2001772.
[14] C. Bi, S. V. Kershaw, A. L. Rogach, J. Tian, *Adv. Funct. Mater.* **2019**, *29*, 1902446.
[15] L. Protesescu, S. Yakunin, S. Kumar, J. Bar, F. Bertolotti, N. Masciocchi, A. Guagliardi, M. Grotevent, I. Shorubalko, M. I. Bodnarchuk, C. J. Shih, M. V. Kovalenko, *ACS Nano* **2017**, *11*, 3119.
[16] M. Lu, J. Guo, S. Sun, P. Lu, X. Zhang, Z. Shi, W. W. Yu, Y. Zhang, *Chem. Eng. J.* **2021**, *404*, 126563.
[17] C. Chen, T. Xuan, W. Bai, T. Zhou, F. Huang, A. Xie, L. Wang, R.-J. Xie, *Nano Energy* **2021**, *85*, 106033.
[18] T. J. Milstein, D. M. Kroupa, D. R. Gamelin, *Nano Lett.* **2018**, *18*, 3792.
[19] F. Liu, Y. Zhang, C. Ding, S. Kobayashi, T. Izuishi, N. Nakazawa, T. Toyoda, T. Ohta, S. Hayase, T. Minemoto, K. Yoshino, S. Dai, Q. Shen, *ACS Nano* **2017**, *11*, 10373.
[20] Q. A. Akkerman, V. D'Innocenzo, S. Accornero, A. Scarpellini, A. Petrozza, M. Prato, L. Manna, *J. Am. Chem. Soc.* **2015**, *137*, 10276.
[21] E. M. Sanehira, A. R. Marshall, J. A. Christian, S. P. Harvey, P. N. Ciesielski, L. M. Wheeler, P. Schulz, L. Y. Lin, M. C. Beard, J. M. Luther, *Sci. Adv.* **2017**, *3*, eaaO4204.
[22] L. Zhang, C. Kang, G. Zhang, Z. Pan, Z. Huang, S. Xu, H. Rao, H. Liu, S. Wu, X. Wu, X. Li, Z. Zhu, X. Zhong, A. K. Y. Jen, *Adv. Funct. Mater.* **2020**, *31*, 2005930.
[23] S. Lim, G. Lee, S. Han, J. Kim, S. Yun, J. Lim, Y.-J. Pu, M. J. Ko, T. Park, J. Choi, Y. Kim, *ACS Energy Lett.* **2021**, *6*, 2229.
[24] Y. K. Wang, F. Yuan, Y. Dong, J. Y. Li, A. Johnston, B. Chen, M. I. Saidaminov, C. Zhou, X. Zheng, Y. Hou, K. Bertens, H. Ebe, D. Ma, Z. Deng, S. Yuan, R. Chen, L. K. Sagar, J. Liu, J. Fan, P. Li, X. Li, Y. Gao, M. K. Fung, Z. H. Lu, O. M. Bakr, L. S. Liao, E. H. Sargent, *Angew. Chem., Int. Ed.* **2021**, *60*, 16164.
[25] J. Xie, P. Hang, H. Wang, S. Zhao, G. Li, Y. Fang, F. Liu, X. Guo, H. Zhu, X. Lu, X. Yu, C. C. S. Chan, K. S. Wong, D. Yang, J. Xu, K. Yan, *Adv. Mater.* **2019**, *31*, 1902543.
[26] M. M. Tavakoli, W. Tress, J. V. Milić, D. Kubicki, L. Emsley, M. Grätzel, *Energy Environ. Sci.* **2018**, *11*, 3310.
[27] Y. Xu, Y. Cui, H. Yao, T. Zhang, J. Zhang, L. Ma, J. Wang, Z. Wei, J. Hou, *Adv. Mater.* **2021**, *33*, 2101090.

© 2021 Wiley-VCH GmbH

[28] L. Sun, L. Bao, B. R. Hyun, A. C. Bartnik, Y. W. Zhong, J. C. Reed, D. W. Pang, H. D. Abruña, G. G. Malliaras, F. W. Wise, *Nano Lett.* **2009**, *9*, 789.
[29] A. Swarnkar, A. R. Marshall, E. M. Sanehira, B. D. Chernomordik, D. T. Moore, J. A. Christians, T. Chakrabarti, J. M. Luther, *Science* **2016**, *354*, 92.
[30] N. C. Anderson, M. P. Hendricks, J. J. Choi, J. S. Owen, *J. Am. Chem. Soc.* **2013**, *135*, 18536.
[31] E. A. Gaulding, J. Hao, H. S. Kang, E. M. Miller, S. N. Habisreutinger, Q. Zhao, A. Hazarika, P. C. Sercel, J. M. Luther, J. L. Blackburn, *Adv. Mater.* **2019**, *31*, 1902250.
[32] J. E. Tackett, *Appl. Spectrosc.* **1989**, *43*, 483.
[33] D. M. Kroupa, M. Vörös, N. P. Brawand, B. W. McNichols, E. M. Miller, J. Gu, A. J. Nozik, A. Sellinger, G. Galli, M. C. Beard, *Nat. Commun.* **2017**, *8*, 15257.
[34] T. Mariappan, Y. Zhou, J. Hao, C. A. Wilkie, *Eur. Polym. J.* **2013**, *49*, 3171.
[35] F. Mangolini, A. Rossi, N. D. Spencer, *J. Phys. Chem. C* **2010**, *115*, 1339.
[36] F. Mangolini, A. Rossi, N. D. Spencer, *J. Phys. Chem. C* **2012**, *116*, 5614.
[37] J. J. Yoo, G. Seo, M. R. Chua, T. G. Park, Y. Lu, F. Rotermund, Y.-K. Kim, C. S. Moon, N. J. Jeon, J.-P. Correa-Baena, V. Bulović, S. S. Shin, M. G. Bawendi, J. Seo, *Nature* **2021**, *590*, 587.
[38] W. Tress, *Adv. Energy Mater.* **2017**, *7*, 1602358.
[39] X. Ling, S. Zhou, J. Yuan, J. Shi, Y. Qian, B. W. Larson, Q. Zhao, C. Qin, F. Li, G. Shi, C. Stewart, J. Hu, X. Zhang, J. M. Luther, S. Duhm, W. Ma, *Adv. Energy Mater.* **2019**, *9*, 1900721.
[40] A. H. Proppe, J. Xu, R. P. Sabatini, J. Z. Fan, B. Sun, S. Hoogland, S. O. Kelley, O. Voznyy, E. H. Sargent, *Nano Lett.* **2018**, *18*, 7052.
[41] F.-C. Chen, J.-L. Wu, C.-L. Lee, Y. Hong, C.-H. Kuo, M. H. Huang, *Appl. Phys. Lett.* **2009**, *95*, 013305.
[42] V. D. Mihailetchi, L. J. Koster, J. C. Hummelen, P. W. Blom, *Phys. Rev. Lett.* **2004**, *93*, 216601.
[43] Y. Xue, F. Yang, J. Yuan, Y. Zhang, M. Gu, Y. Xu, X. Ling, Y. Wang, F. Li, T. Zhai, J. Li, C. Cui, Y. Chen, W. Ma, *ACS Energy Lett.* **2019**, *4*, 2850.
[44] J. Tian, Q. Xue, X. Tang, Y. Chen, N. Li, Z. Hu, T. Shi, X. Wang, F. Huang, C. J. Brabec, H.-L. Yip, Y. Cao, *Adv. Mater.* **2019**, *31*, 1901152.
[45] S. S. Hegedus, W. N. Shafarman, *Prog. Photovoltaics* **2004**, *12*, 155.
[46] Y. Wang, C. Duan, X. Zhang, N. Rujisamphan, Y. Liu, Y. Li, J. Yuan, W. Ma, *ACS Appl. Mater. Interfaces* **2020**, *12*, 31659.
[47] J. Shi, J. Dong, S. Lv, Y. Xu, L. Zhu, J. Xiao, X. Xu, H. Wu, D. Li, Y. Luo, Q. Meng, *Appl. Phys. Lett.* **2014**, *104*, 063901.
[48] Y. Wang, C. Duan, J. Li, W. Han, M. Zhao, L. Yao, Y. Wang, C. Yan, T. Jiu, *ACS Appl. Mater. Interfaces* **2018**, *10*, 20128.
[49] S. Bag, O. Gunawan, T. Gokmen, Y. Zhu, T. K. Todorov, D. B. Mitzi, *Energy Environ. Sci.* **2012**, *5*, 7060.
[50] T. He, S. Li, Y. Jiang, C. Qin, M. Cui, L. Qiao, H. Xu, J. Yang, R. Long, H. Wang, M. Yuan, *Nat. Commun.* **2020**, *11*, 1672.
[51] A. Yella, L. P. Heiniger, P. Gao, M. K. Nazeeruddin, M. Grätzel, *Nano Lett.* **2014**, *14*, 2591.

© 2021 Wiley-VCH GmbH